ACS Catalysis

Research Article

Cite This: ACS Catal. 2019, 9, 8702−8711

pubs.acs.org/acscatalysis

Unlocking the Potential of Nanoparticles Composed of Immiscible Elements for Direct H_2O_2 Synthesis

Donghun Kim,[†,#] Hyobin Nam,[‡,§,#] Young-Hoon Cho,[∥,#] Byung Chul Yeo,[†,#] So-Hye Cho,[‡] Jae-Pyung Ahn,[⊥] Kwan-Young Lee,[*,∥] Seung Yong Lee,[*,‡,§] and Sang Soo Han[*,†]

[†]Computational Science Research Center, Korea Institute of Science and Technology, Seoul 02792, Republic of Korea

[‡]Materials Architecturing Research Center, Korea Institute of Science and Technology, Seoul 02792, Republic of Korea

[§]Department of Nanomaterials Science and Engineering, Korea University of Science and Technology, Daejeon 34113, Republic of Korea

[∥]Department of Chemical and Biological Engineering, Korea University, Seoul 02841, Republic of Korea

[⊥]Advanced Analysis Center, Korea Institute of Science and Technology, Seoul 02792, Republic of Korea

Supporting Information

ABSTRACT: Today, multimetallic nanoparticles (NPs) are extensively studied to search for high-performance catalysts. Unfortunately, a huge material space of NPs composed of immiscible elements has been generally disregarded for catalyst development due to the inherent difficulty of alloy synthesis. Herein, for the direct synthesis of hydrogen peroxide (H_2O_2), we demonstrate that NPs of immiscible elemental combinations of Rh−Ag, Rh−Au, Pt−Au, and Ir−Ag can efficiently produce H_2O_2, despite the negligible activities of Rh, Pt, Ir, Ag, and Au alone. In particular, we show that two catalysts, $Rh_{13}Ag_{87}$ and $Pt_{28}Au_{72}$ NPs, can outperform prototypic Pd NPs. $Rh_{13}Ag_{87}$ NPs, owing to their high content of the less-expensive element Ag, exhibit a 7.3-fold enhancement in cost-normalized productivity compared to Pd and, thus, may serve as an economical option. The other catalyst of $Pt_{28}Au_{72}$ NPs exhibits a productivity of 300 mmol g_{cat}^{-1} h^{-1} and a 15-fold increase over that of Pd under isoconversion conditions. The observed remarkable productivities of these NPs are a result of the synergy between the two elemental domains at the interface. The present study suggests that the hitherto underutilized space of immiscible elemental combinations should be more actively searched for the development of improved catalyst materials.

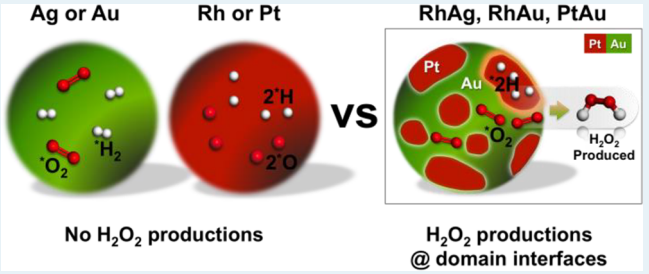

KEYWORDS: *bimetallic catalysts, metal nanoparticles, immiscible elements, Rh−Ag, Pt−Au, hydrogen peroxide direct synthesis, interfacial reactions, DFT calculations*

1. INTRODUCTION

Copious amounts of hydrogen peroxide (H_2O_2) are produced globally.[1] The demand is currently met by an indirect process in which anthraquinone molecules are sequentially hydrogenated and oxidized in large-scale facilities.[2,3] The anthraquinone process, however, produces concentrated H_2O_2, resulting in associated storage and transport hazards. In reality, many applications, including bleaching and water purification, require only dilute H_2O_2 solutions on a small scale. The direct synthesis of H_2O_2 from molecular H_2 and O_2 is a more suitable solution to meet these demands because this process can be easily conducted at the consumption point.

Palladium (Pd) has been used as an efficient catalyst for direct H_2O_2 synthesis since the earliest patents were filed in 1914.[4−6] Recently, extensive efforts have been devoted to discovering multimetallic catalysts with better performances than monometallic Pd catalysts, and a markedly enhanced activity or selectivity has been observed for Pd−Au,[2,7−11] Pd−Pt,[12] and Pd−Sn[13] alloy catalysts. These high-performance bimetallic catalysts are mostly based on miscible elemental combinations (negative bulk formation energy),[2,7−15] in which the intermixing of two elements is thermodynamically favorable, i.e., the two elements are homogeneously mixed at the atomic level.

The traditional "mixing" approach may have led the research community to overlook a large material space, namely, nanoparticles (NPs) composed of immiscible elements, which have little or no intermixing between the two elements. This material space has been largely unexplored yet, mainly for two reasons: (1) intermixing of bulk-immiscible elements is inherently difficult, and (2) little intermixing is believed to cause minimal changes in catalytic performances from monometallic cases. Here, we show that even materials in the underutilized space of immiscible elemental combinations

Received: January 31, 2019
Revised: July 26, 2019
Published: August 9, 2019

DOI: 10.1021/acscatal.9b00451
ACS Catal. 2019, 9, 8702−8711

can perform very differently from monometallic ones. We demonstrate that novel catalysts including $Rh_{13}Ag_{87}$ NPs or $Pt_{28}Au_{72}$ NPs (immiscible elements for both) significantly outperform the prototypic Pd in H_2O_2 productions, despite the negligible activity of Rh, Ag, Pt, and Au NPs alone. Density functional theory (DFT) calculations and experimental spectroscopies reveal that the observed remarkable productivities arise from the synergy between two elemental domains at interfaces.

2. METHODS

2.1. Density Functional Theory Calculations. All the calculations were performed using the Vienna Ab Initio Simulation Packages (VASP)[16] with the revised Perdew–Burke–Ernzerhof (RPBE)[17] functional as the exchange and correlation functional. The projector-augmented-wave method was adopted to describe the potential from the ionic core.[18] An energy cutoff of 480 eV was used. For formation energy calculations of bulk materials, a Monkhorst–Pack *k*-point sampling of 8 × 8 × 8 was used. For slab calculations, *k*-point sampling of 4 × 4 × 1 was used. A large vacuum spacing, >15 Å, was used to prevent interslab interactions. In the simulations, (111) surfaces are investigated given our experimental observation that the synthesized NPs are all spherical-shaped and also given the fact that (111) is the most stable surface type for face-centered cubic (FCC) metals (Rh, Ir, Pt, Ag, Au, and Pd). Each (111) surface was modeled by a supercell slab that consisted of a 3 × 3 surface unit cell with four single layers. The top two layers and the reactant molecules were fully relaxed until the maximum Hellmann–Feynman forces were <0.05 eV $Å^{-1}$. In addition, a transition state for each reaction on the metal surfaces was found using the climbing-image nudged elastic band (CI–NEB) method.[19]

2.2. Chemicals. Rhodium(III) acetate [$Rh(CH_3COO)_3$, 99.95%] was purchased from DONG JIN PGMs Chemical Company. Poly(vinylpyrrolidone) (PVP, MW = 55 000), gold(III) chloride trihydrate [$HAuCl_4{\cdot}3H_2O$, 99.9%], iridium(III) chloride hydrate [$IrCl_3{\cdot}xH_2O$, 99.9%], platinum(II) acetylacetonate [$Pt(acac)_2$, 97%], and sodium borohydride [$NaBH_4$, 98%] were purchased from Sigma-Aldrich. Silver nitrate [$AgNO_3$, 99.995%] was purchased from Alfa Aesar, and ethylene glycol was purchased from Junsei. 1,5-Pentanediol was purchased from ACROS. All solvents, including acetone, ethanol, hexane, and chloroform, were analytical grade and were used without further purification.

2.3. Catalyst Synthesis. NPs were mainly synthesized using the polyol reduction method. PVP (0.763 g) was dissolved in 100 mL of ethylene glycol, and the temperature was brought to 170 °C in air under magnetic stirring (500 rpm). Then, 0.05 mmol of metal precursors in total was dissolved in 10 mL of deionized water and injected into the hot ethylene glycol/PVP solution at once. The synthetic procedure of PtAu NPs slightly differs from the others. PVP (0.76 g) was dissolved in 100 mL of 1,5-pentanediol (instead of ethylene glycol), and the temperature was brought to 187 °C in air under magnetic stirring (500 rpm). After 30 min, 0.025 mmol of $Pt(acac)_2$ was dissolved in 0.5 mL of chloroform and 4.5 mL of 1,5-pentanediol, and 0.025 mmol of $HAuCl_4{\cdot}3H_2O$ was dissolved in 5 mL of deionized water. The reason for using 1,5-pentanediol for the PtAu case is that $Pt(acac)_2$ was dissolved in chloroform because of low solubility in deionized (DI) water, as well as the fact that chloroform can be homogeneously mixed with pentanediol, compared to ethylene glycol. The Pt solution was injected into the hot 1,5-pentanediol/PVP solution, and then the Au solution was injected quickly. The molar ratio of the initially loaded metal elements is summarized as follows: Rh/Ag = 5/95 (5/95), 10/90 (13/87), 30/70 (26/74), 65/35 (50/50), and 80/20 (69/31); Rh/Au = 50/50 (46/54); Pt/Au = 10/90 (8/92), 30/70 (28/72), and 50/50 (42/58); Ir/Ag = 50/50 (18/82); and Ir/Au = 50/50 (10/90). The ratio in parentheses is the real catalytic ratio determined from inductively coupled plasma (ICP) measurements. To ensure zero activities of some pure NPs synthesized from the polyol reduction experiments, pure Ag, Au, and Rh NPs were tested via additional route, namely, $NaBH_4$ reduction method reported by Solomon and coworkers,[20] which allows for synthesizing relatively smaller particles. PVP (0.153 g) and 0.012 g of $NaBH_4$ were dissolved in 15 mL of deionized water. Meanwhile, 0.01 mmol of metal precursors in total were dissolved in 5 mL of deionized water. The aqueous solution was added dropwise to deionized water containing PVP and $NaBH_4$ in an ice-water bath. A typical synthesis of Pd NPs was reported by Jin et al.[21] First, Na_2PdCl_4 solution was prepared by dissolving 44.5 mg of $PdCl_2$, 0.5 mL of 1 M HCl, 0.5 mL of 1 M NaOH, and 2.866 mL of deionized water. PVP (11 mg), 60 mg of acrylic acid (AA), and 300 mg of KBr were dissolved in 8 mL of deionized water and preheated in air under magnetic stirring (500 rpm) at 80 °C for 10 min. Then, 3 mL of Na_2PdCl_4 solution was added. After the vial was capped, the reaction was allowed to proceed at 80 °C for 3 h. The Pd NPs were washed with deionized water by ultracentrifugation (13 500 rpm). The resulting catalyst NPs (except Pd NPs) were purified by an initial precipitation with acetone and isolated by ultracentrifugation (10 000 rpm). Two cycles of redispersion in ethanol and reprecipitation with hexane followed by centrifugal isolation were then employed to remove excess PVP. The IrAg NPs were filtered to remove the AgCl NPs.

2.4. Catalyst Characterization. Transmission electron microscopy (TEM) images and energy-dispersive X-ray spectra (EDS) were acquired using a transmission electron microscope (FEI Talos F200X) equipped with scanning transmission electron microscopy–energy-dispersive X-ray spectroscopy (Bruker Super–X EDS system). The crystal structure was examined by X-ray diffraction (XRD) with Cu Kα radiation (λ = 1.5406 Å). The samples for the TEM images and XRD spectra were purified by centrifugation four times to remove the surfactants and/or excess reactants. Then, the NPs were dispersed in ethanol. The resulting solution was dropped on a copper grid coated with an amorphous carbon film for the TEM images and a Si wafer for the XRD spectra.

2.5. Catalyst Performance Measurements. The direct synthesis of H_2O_2 was performed in a double-jacket glass reactor under stirring at 1200 rpm. The reaction medium (150 mL) was composed of ethanol and water (ethanol/water volume ratio = 1:4) with 0.9 mM potassium bromide (KBr) and 0.03 M phosphoric acid (H_3PO_4). The used catalyst weight for RhAg NPs was in the range of 4.9–6.5 mg (slightly varying with compositions); for RhAu NPs, it was 6.6 mg; for IrAg NPs, it was 2.0 mg; and for PtAu NPs, it was 1.7 mg. The catalyst weight for each catalytic sample is available in Table S1. The reason for the different masses of loaded metals is the different synthesis yield for each material. Different masses, however, have little effect on the quantities of H_2O_2 productivity, as it is calculated in a mass normalized unit (mmol/g_{cat} h). The volumetric flow rate of the reactant gas

DOI: 10.1021/acscatal.9b00451
ACS Catal. 2019, 9, 8702–8711

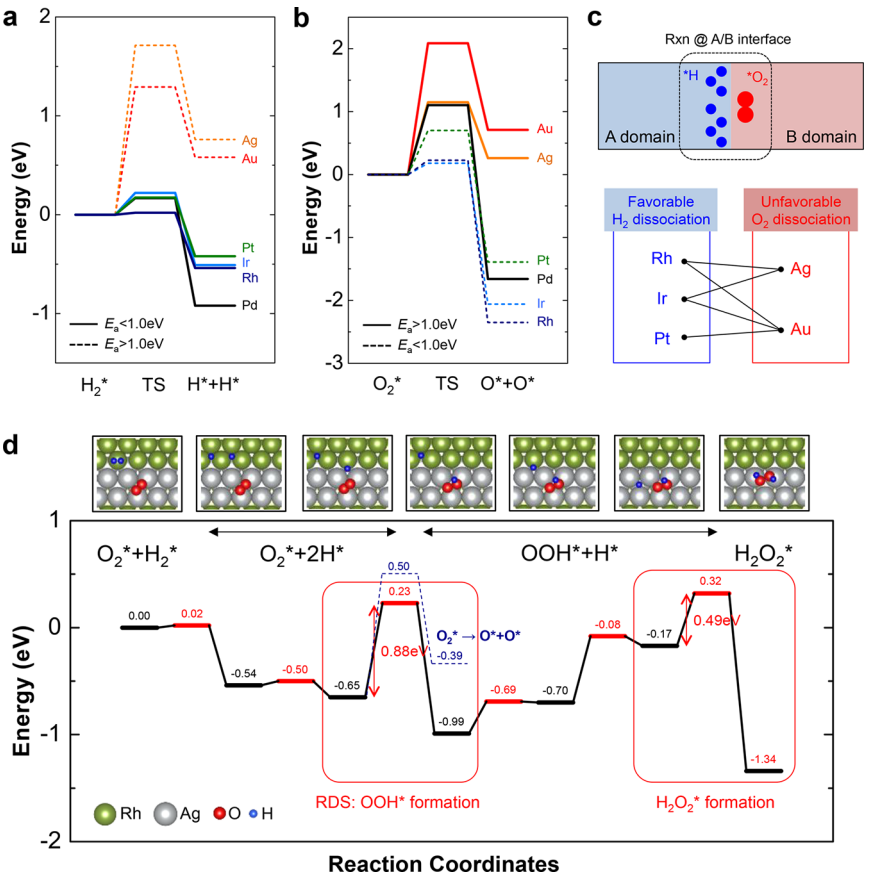

Figure 1. DFT-calculation-guided development of the catalyst design strategy. (a, b) Calculated energetics of H_2 and O_2 dissociative adsorptions on the (111) surface of six single-element FCC (face-centered cubic) metals (i.e., Rh, Ir, Pt, Ag, Au, and Pd). (c) Schematic of the surface of the bimetallic **AB** catalysts where the **A**/**B** interface is proposed to serve as the H_2O_2 production site. Candidate elements for **A** and **B** and their immiscible combinations are shown. (d) Energy levels and corresponding geometries [(111) surface exposed, top view] during the synthesis of a H_2O_2 molecule at a Rh/Ag interface, where the asterisks indicate the surface species.

stream was 22 mL/min (H_2/O_2 volume ratio = 1:10). The flammability limit for H_2 in O_2 (at 20 °C, 1 atm) is 4−94%,[22] and thus, our 10% mixture is within the flammable regime. To prevent associated potential hazards, care should be taken to avoid contact between the gas mixture and the dry catalysts.[15,23] It should be noted that the gas mixture was fed into the aqueous solution that remained in the reactor. In the absence of such aqueous reaction conditions, a more dilute gas mixture (<4% H_2 in O_2) is desired to prevent any possible hazards. The reaction was performed at 293 K and 1 atm for 1 h, except for in the long-term stability tests (up to 18 h). Note that the recyclability test of $Pt_{28}Au_{72}$/silica catalyst was performed under the same reaction conditions with the fresh catalyst cases. After the reaction, the concentration of H_2O_2 was calculated using iodometric titration. The concentration of H_2 was calculated using gas chromatography (Younglin, ACME6000) equipped with a Carbosieve SII (60−80 mesh) packed column and a thermal conductivity detector (TCD).

3. RESULTS AND DISCUSSION

3.1. DFT Calculation-Guided Development of Catalyst Design Strategy. The first step toward the design of potential bimetallic catalysts is to sensibly select the elements and their combinations. There are two requirements for a catalyst for efficient H_2O_2 synthesis: (1) favorable H_2 dissociation and (2) unfavorable O_2 dissociation.[24] On the basis of the literature, we chose Rh, Ir, and Pt as the elements to meet the first requirement (i.e., favorable H_2 dissociation)[25,26] and Ag and Au as the elements to meet the second requirement (i.e., unfavorable O_2 dissociation).[27]

To confirm our element selections, using *ab initio* density functional theory (DFT) calculations, we investigated the energetics of H_2 and O_2 dissociative adsorption on the (111) surfaces of these five pure metals (Rh, Ir, Pt, Ag, and Au), using Pd as a reference material (Figure 1a and b). As expected, Pd(111) fulfills both requirements. H_2 dissociation occurs with a low activation energy (0.17 eV), and in contrast, the energy barrier for O_2 dissociation (1.10 eV) is high enough to prevent its occurrence at room temperature. Unlike Pd, the other five metals satisfy only one of the two requirements. With Ag and Au, for instance, O_2 dissociation is desirably prevented owing to both of the high energy barriers (1.15 and 2.09 eV, respectively) and the endothermic properties, in agreement with previous reports.[27−30] However, H_2 dissociation will also not occur due to the high energy barriers (1.71 and 1.29 eV, respectively). For the other metals (Rh, Ir, and Pt), both O_2 and H_2 dissociations are likely to occur with ease due to the relatively low energy barriers (<0.2 eV in most cases). This finding explains well the previous experimental observations[3,31] as well as our own (Figures S1−S3 and Table S2 in the Supporting Information) that single-element metal NPs (except for Pd) exhibit negligible catalytic performance for H_2O_2 synthesis.

DOI: 10.1021/acscatal.9b00451
ACS Catal. 2019, 9, 8702−8711

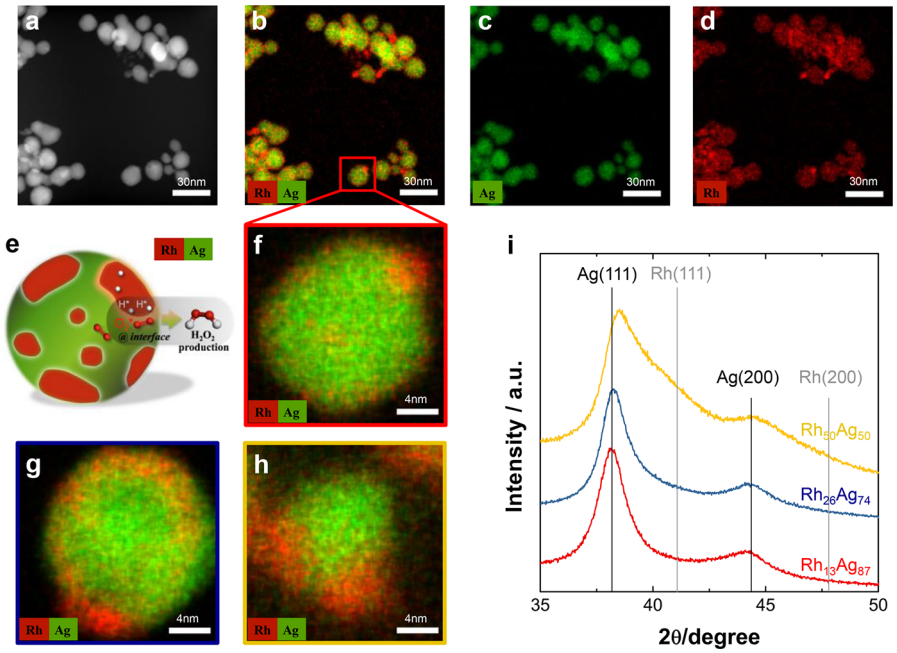

Figure 2. Structural analysis of the RhAg NPs. (a–d) Representative high-angle annular dark-field (HAADF) grayscale image and the corresponding EDS (RGB) maps of the collective $Rh_{13}Ag_{87}$ NPs. The qualitative elemental distributions of Rh and Ag are represented by red and green, respectively. (e) Schematic describing the H_2O_2-producing mechanism on RhAg surfaces. (f–h) Magnified EDS images capturing a single NP for (f) $Rh_{13}Ag_{87}$, (g) $Rh_{26}Ag_{74}$, and (h) $Rh_{50}Ag_{50}$. (i) XRD patterns of RhAg NPs with different compositions.

NPs composed of immiscible elements may benefit from the synergy of each element. The design strategy is as follows. For the **AB** bimetallic catalyst depicted in Figure 1c, the **A** domain offers facile H_2 dissociation, and the **B** domain suppresses O_2 dissociation; therefore, H_2O_2 can be produced at the **A**/**B** interface. Our calculations predicted the candidate elements for **A** to be Rh, Ir, and Pt and those for **B** to be Ag and Au, resulting in a total of five immiscible combinations, i.e., Rh–Ag, Rh–Au, Pt–Au, Ir–Ag, and Ir–Au. Note that Pt and Ag are known to form miscible alloy NPs,[32,33] and thus, the Pt–Ag combination was not of interest in the present work.

To ensure that the suggested interfacial reaction is feasible, we investigated the energetics of a full surface reaction path (i.e., $O_2^* + H_2^* \rightarrow H_2O_2^*$) using the Rh–Ag combination as an example (Figure 1d), where * indicates metal surface sites. In the model, O_2 and H_2 molecules sit on the Ag and Rh sides, respectively, but both are in the immediate vicinity of the Rh/Ag interface so that the synthesis can be initiated. The initial geometry of O_2 on Ag and H_2 on Rh was justified from a kinetics viewpoint. H_2 molecules are well-known to diffuse much faster than O_2 molecules because of their much smaller mass,[34] and as a result, exposed Rh domains are predominantly covered by H_2 molecules. Under the circumstance of Rh domains being dominated by H_2 species, O_2 molecules would reach to Ag domains, causing O_2 (Ag)–H_2 (Rh) configurations to most likely occur. The adsorbent coverage is chosen as that in which the adsorption energy per O_2–H_2 pair is the lowest (Tables S3 and S4 in the Supporting Information).

The key results are as follows: (1) the full reaction at the Rh/Ag interface is predicted to be overall exothermic by 1.34 eV and (2) undesirable O_2 dissociation can be prevented because the barrier of OOH* formation (0.88 eV) is lower than that of O_2 dissociation (1.15 eV). It is worth noting that the barrier height of OOH* formation is even smaller than that on the well-known Pd(111) surface (0.91 eV),[24] indicating that the suggested reaction is likely to occur at the Rh/Ag interface. The proposed reaction sites are the Ag metal atoms in the immediate vicinity of a Rh/Ag interface, and this site offers two benefits for H_2O_2 production: (1) O_2 dissociation can be prevented due to the oxophobic nature of Ag and (2) the dissociated H atoms can diffuse from the neighboring Rh domain.

3.2. H_2O_2 Production from Rh/Ag Interfaces. Motivated by the computational predictions, we synthesized RhAg NPs using a polyol reduction method,[35] characterized the structures, and tested their catalytic performances for direct H_2O_2 synthesis. A variety of Rh/Ag compositions, including 5:95, 13:87, 26:74, 50:50, and 69:31, were considered. TEM images of the RhAg NPs are shown in Figure 2a–h with different length scales and mapping methods. For all the compositions tested, each Ag and Rh domain is clearly observed, and the domains are separated instead of homogeneously alloyed because Rh and Ag are thermodynamically immiscible[25] (Figure S4 in the Supporting Information). Because of the higher reduction potential of Ag relative to Rh,[36] Ag tends to nucleate before Rh, forming the core of the NPs, and Rh islands of different sizes sit on the Ag cores in a random manner (Figure 2f–h). Such NP structures are also consistent with the EDS line-scan results where Ag profiles are Gaussian-distribution-like, and Rh profiles irregularly fluctuate regardless of scanning directions (Figure S5 in the Supporting Information). As a result, a number of Rh/Ag interfaces form on the NP surfaces and can serve as reaction sites for H_2O_2 production, as our calculations predicted (Figure 1d).

Because TEM-EDS maps and the line scans locate a few local spots of potential Rh–Ag alloying in RhAg NPs, XRD patterns are obtained to assess whether the alloying of two elements occurred in our samples. From the comparison of dominant peak positions and those of the reference Ag, we

DOI: 10.1021/acscatal.9b00451
ACS Catal. 2019, 9, 8702–8711

Table 1. Catalytic Performances of the RhAg NPs in Comparison to Those of Pure Ag, Rh, and Pd Metals[a]

catalyst		H_2O_2 productivity			H_2 conversion (%)	H_2O_2 selectivity (%)
		mass normalized (mmol g_{cat}^{-1} h^{-1})	interface-length normalized ($\times 10^{-19}$ mmol nm^{-1} h^{-1})	cost normalized (mmol $\$_{cat}^{-1}$ h^{-1})		
Ag NPs		0	0	0	0	0
Rh NPs		0	0	0	0.4	0
RhAg NPs	Rh_5Ag_{95}	0	0	0	0.2	0
	$Rh_{13}Ag_{87}$	67	1.9 (±0.6)	13.3	3.2	62
	$Rh_{26}Ag_{74}$	30	1.4 (±0.4)	2.1	2.4	78
	$Rh_{50}Ag_{50}$	8	0.8 (±0.2)	0.3	5.1	16
	$Rh_{69}Ag_{31}$	0	0	0	0.4	0
Pd NPs		59	N/A	1.8	11.7	39

[a]The H_2O_2 productivity is shown in three normalization schemes, namely, based on catalyst mass, interface length, and cost, for different purposes. Reactions were carried out under the following conditions: *T*, 20 °C; *P*, 1 atm; reaction medium, 150 mL of a DI water mixture (20% ethanol, 0.9 mM KBr, and 0.03 M H_3PO_4); reaction time, 1 h; total flow rate, 22 mL/min; H_2/O_2, 1/10.

observe that Rh−Ag partial alloying likely exists at the nanoscale and increases with Rh content. In particular, in Rh-rich (Rh ≥ 50%) samples including $Rh_{50}Ag_{50}$ NPs, a clear peak shift was observed in the XRD results (Figure S7). For instance, the Ag(111) peak is shifted by +0.3° and the Rh(111) peak is shifted by −1.3°, as confirmed by XRD deconvolution analysis in Figure S8. In addition, the XPS spectra are obtained to probe the oxidation states, and they reveal that Rh elements in RhAg NPs dominantly exist in the metallic Rh^0 state but partly exist in the oxidized Rh^{3+} state, as in Rh_2O_3 (Figures S9 and S10).

The RhAg NPs exhibit H_2O_2 production rates comparable to the reference Pd catalyst (Table 1). In particular, among the several compositions of our investigation, the Ag-rich $Rh_{13}Ag_{87}$ sample shows the largest productivity of 67 mmol g_{cat}^{-1} h^{-1}, which is comparable to that of Pd NPs (59 mmol g_{cat}^{-1} h^{-1}). The productivity of Rh_xAg_{1-x} NPs monotonically declines with increasing Rh content, reaching zero at $x = 0.69$. For our own Pd samples, the use of SiO_2 support slightly modifies the H_2O_2 productivity and the selectivity, by only 18% and 7%, respectively[37] (Table S5 in the Supporting Information). Note that the reported productivity values for Pd NPs of similar size and shape range between 30 and 86 mmol g_{cat}^{-1} h^{-1}; our own value is also placed within this range (Table S6 and Figure S11 in the Supporting Information).[3,37,38] The H_2O_2 degradation tests were also performed, and the degradation activity of $Rh_{13}Ag_{87}$ NPs was measured to be only 177 mmol g_{cat}^{-1} h^{-1} under inert atmosphere (Figure S12 in the Supporting Information), which is lower than that of our Pd reference (455 mmol g_{cat}^{-1} h^{-1}, Figure S12 in the Supporting Information) as well as that reported for Au−Pd (235 mmol g_{cat}^{-1} h^{-1}).[39,40]

The H_2O_2 productivities of RhAg NPs are enabled by the synergistic effect at the Rh/Ag interfaces, because pure Rh and Ag NPs cannot produce H_2O_2. To support this standpoint, estimations of interfacial length and their relation to productivity are necessary. For this purpose, we developed a simple model to estimate the quantities of interfacial length in each sample (Figure S13 and Table S7). As a result of this modeling, we reveal that, as Rh content increases ($Rh_{13}Ag_{87}$ → $Rh_{26}Ag_{74}$ → $Rh_{50}Ag_{50}$), the average Rh domain size also increases (0.60 → 1.10 → 2.26 nm in diameter measures), which leads to the monotomic decrease of interfacial length. This result quantitatively explains the decrease of H_2O_2 productivity with increasing Rh content and, thus, supports that the observed productivity mainly arises from the interface effects. We introduce a new metric, i.e., the interface-length normalized productivity (INP; unit, mmol nm^{-1} h^{-1}). Note the replacement of the mass [unit, gram (g)] with the estimated interfacial length [unit, nm]. INP values, serving as a kind of intrinsic activity, of $Rh_{13}Ag_{87}$ and $Rh_{26}Ag_{74}$ NPs are similar (Table 1), which supports that the interface effect is the major production mechanism. We importantly note that the INP of $Rh_{50}Ag_{50}$ NPs is worse than those of low Rh content samples. This is likely due to the fact that partial Rh−Ag alloying in $Rh_{50}Ag_{50}$ may hinder O_2 stabilization on surfaces (proven by DFT calculations in Figure S14), which should additionally contribute to the activity drop.

To assess the cost-effectiveness of the RhAg catalysts, we introduced another productivity metric, i.e., the cost-normalized productivity (CNP; unit, mmol $\$_{cat}^{-1}$ h^{-1}). Note that we used the metal price [unit, U.S. dollar ($)] instead of catalyst mass [unit, gram (g)]. In this new metric, RhAg catalysts are even more attractive due to the lower cost of Ag metal. Ag and Rh are ∼59-fold less expensive and 1.4-fold more expensive than Pd, respectively;[41] thus, a higher Ag content in the RhAg NPs results in less-expensive catalysts. In particular, among the tested samples, $Rh_{13}Ag_{87}$ NPs serve as the most cost-effective option owing to their low Rh content, and they exhibit an ∼7.3-fold enhanced CNP value (13.29 mmol $\$_{cat}^{-1}$ h^{-1}) compared to Pd NPs.

3.3. General Expansions to Other Immiscible Elemental Combinations. Having demonstrated the catalytic activities of the RhAg NPs, we expanded our design strategy to examine the other four immiscible cases (Rh−Au, Pt−Au, Ir−Ag, and Ir−Au) suggested in Figure 1c. We synthesized bimetallic NPs of these four elemental combinations and characterized the structures. Note that, while only a single composition was considered for RhAu ($Rh_{46}Au_{54}$), IrAg ($Ir_{18}Ag_{82}$), and IrAu ($Ir_{10}Au_{90}$), three different compositions (Pt/Au = 8:92, 28:72, and 42:58) were investigated for PtAu NPs to achieve the best catalytic performance. The TEM images shown in Figure 3a−d reveal that the structures of the RhAu and PtAu NPs are very similar to those of the RhAg NPs. Au dominates the core of the NPs, and a number of Rh or Pt islands form on the surfaces (Figure S15 in the Supporting Information). It is important to note that Au salts are more readily reduced than the counterpart elements (Rh or Pt) because of their higher reduction potentials[36] and, thus, form the seeds of the NPs. The structural separation of the two elemental domains is additionally supported by the corresponding XRD spectra (Figure 3g). The dominant peaks align

DOI: 10.1021/acscatal.9b00451
ACS Catal. 2019, 9, 8702−8711

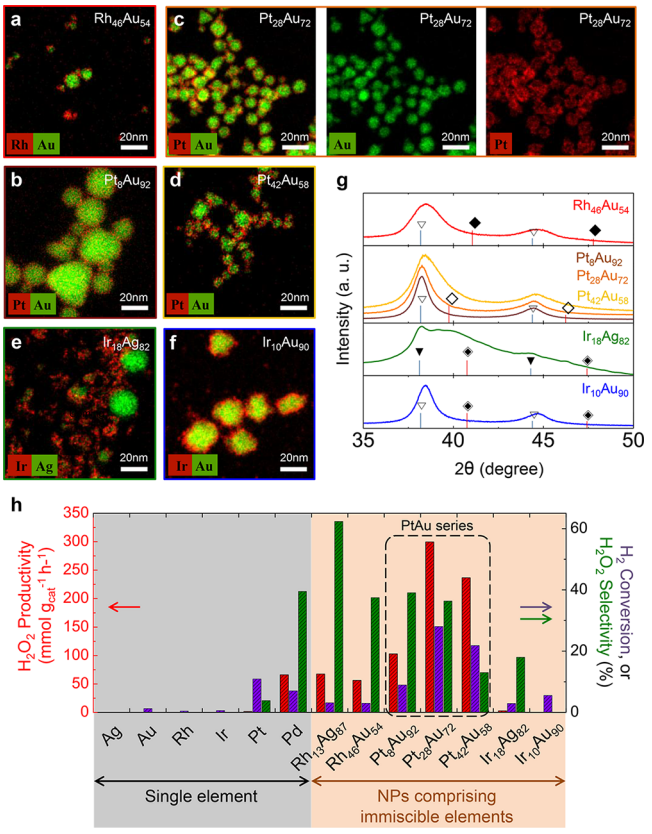

Figure 3. Demonstration of the design strategy for other immiscible elemental combinations. (a–f) EDS (RGB) maps of (a) $Rh_{46}Au_{54}$, (b) Pt_8Au_{92}, (c) $Pt_{28}Au_{72}$, (d) $Pt_{42}Au_{58}$, (e) $Ir_{18}Ag_{82}$, and (f) $Ir_{10}Au_{90}$ NPs. (g) XRD patterns of these catalytic NPs. (h) Catalytic performances (H_2O_2 productivity, selectivity, and H_2 conversion) of the bimetallic catalysts developed in our design scheme in comparison to those of the single-element metals.

with the pure Au peaks, indicating that homogeneous mixtures of Au and the counterpart element (Rh or Pt) did not form. However, it is observed that, as either the Rh or Pt content increases (42% or above), the Au(111) peak slightly shifts toward larger angles. The shift is, however, too small to represent full alloying, thus indicating that partial alloying of the two elements may have occurred at the nanoscale in the high Rh- or Pt-content samples.

The RhAu and PtAu NPs exhibit comparable (56 mmol g_{cat}^{-1} h^{-1}) and much higher (103–300 mmol g_{cat}^{-1} h^{-1}) production rates, respectively, relative to the reference Pd NPs (Figure 3h). It is worth noting that the Au-rich $Pt_{28}Au_{72}$ sample offers the largest productivity of 300 mmol g_{cat}^{-1} h^{-1} among all tested samples. These values are indeed remarkable given the negligible activity of Rh, Pt, and Au NPs alone. In this immiscible NP design scheme, the composition control tests of the RhAg and PtAu series reveal that Ag- or Au-rich compositions lead to the enhanced productivity, likely due to the increased interfacial area (i.e., number of reaction sites). PtAu NPs continue to appear as an attractive option in the CNP unit. $Pt_{28}Au_{72}$ and $Pt_{42}Au_{58}$ NPs exhibit CNP values of 8.0 and 6.6 mmol $\$_{cat}^{-1}$ h^{-1}, respectively, which are 4.3- and 3.6-fold greater than the CNP value of the Pd NPs.

In contrast, the IrAg and IrAu NPs did not perform well for H_2O_2 synthesis, with productivities of 13 and 0 mmol g_{cat}^{-1} h^{-1}, respectively. Such poor activity can be explained by structural factors. For IrAg, Ir and Ag tend to be separated to such an extent that single-element NPs mostly formed (Figure 3e). For IrAu, core (Au)–shell (Ir)-type NPs developed (Figure 3f). In both cases, it is highly unlikely that interfaces between two elemental domains exist on the NP surfaces. In particular, there would be no accessible interface for the core–shell-type configuration, as it is buried, which adequately explains the nonexistent activity of the IrAu NPs. These examples of Ir-based NPs prove that elemental combinations should be carefully chosen to avoid too much separation or core–shell-type particles.

3.4. Isoconversion Comparison and Long-Term Stability and Recyclability. As our new catalysts exhibit a wide range of H_2 conversions (3–28%), it is difficult to perform an accurate comparison of the performance metrics with those of the reference Pd. Experiments at isoconversion are key to conclusively proving that the newly proposed bimetallic NPs are more productive or selective than monometallic Pd. Because of the observed high activities (Figure 3h), PtAu NPs of all three compositions (Pt/Au = 8:92, 28:72, and 42:58) were selected for further isoconversion tests, and their H_2 conversion levels were controlled to reach ~12% (the conversion value of Pd). We observe in Figure 4a that, at the fixed H_2 conversion of 12%, the PtAu NPs become even more fascinating catalysts. In particular, the best catalyst of $Pt_{28}Au_{72}$ NPs exhibits a surpassing productivity of 878 mmol g_{cat}^{-1} h^{-1}, which is 15-fold larger than that of Pd (59 mmol $g_{cat}^{-1}h^{-1}$). In addition, at this conversion, $Pt_{28}Au_{72}$ NPs show a higher selectivity of 56% compared with Pd (39%).

The long-term stability and recyclability have also been taken into account. The catalyst of $Pt_{28}Au_{72}$ NPs is again selected for these stability investigations because of its superior H_2O_2 productivity. Figure 4b shows the accumulated concentration of H_2O_2 produced over time (up to 18 h) with $Pt_{28}Au_{72}$ NPs. One can observe that the H_2O_2 concentration monotonically increases with time, which suggests the long lifetime (over 18 h) of this catalyst. It should also be noted that the accumulation slows over time, indicating that the produced H_2O_2 partially decomposes. The phenomenon of the decreasing speed of H_2O_2 accumulation is generally observed even for state-of-the-art catalysts, including Pd and Au–Pd,[15,40] and is not at all a result of any morphological changes in the catalyst materials. A morphology comparison of $Pt_{28}Au_{72}$ NPs before and after the 18 h reaction (insets of Figure 4b) further reveals that the NP size distributions, shapes, compositions, and degrees of Pt–Au immiscibility barely changed after the reaction, thus supporting the long lifetime (over 18 h) of the new catalysts. The recycle tests were also performed with the most active species of $Pt_{28}Au_{72}$ NPs. The catalyst was consecutively collected and reused over three times of reactions. Figure 4c shows the corresponding H_2O_2 productivity and selectivity in a normalized unit at the first cycle value. Some degrees of fluctuations in catalytic properties are observed between runs. At the second run, each productivity and selectivity are enhanced by 3% and 37%, respectively. At the third run, each property is decreased by 15% and 30%, respectively. The reuse tests reveal that the catalyst is able to produce H_2O_2 over multiple reaction cycles but with up to ±37% fluctuations in catalytic performance.

3.5. Positioning Our Catalysts in Bimetallic Catalyst Map. Figure 5a is the bimetallic catalyst map based on alloy formation energies (E_f), which includes 4 350 DFT calcu-

DOI: 10.1021/acscatal.9b00451
ACS Catal. 2019, 9, 8702–8711

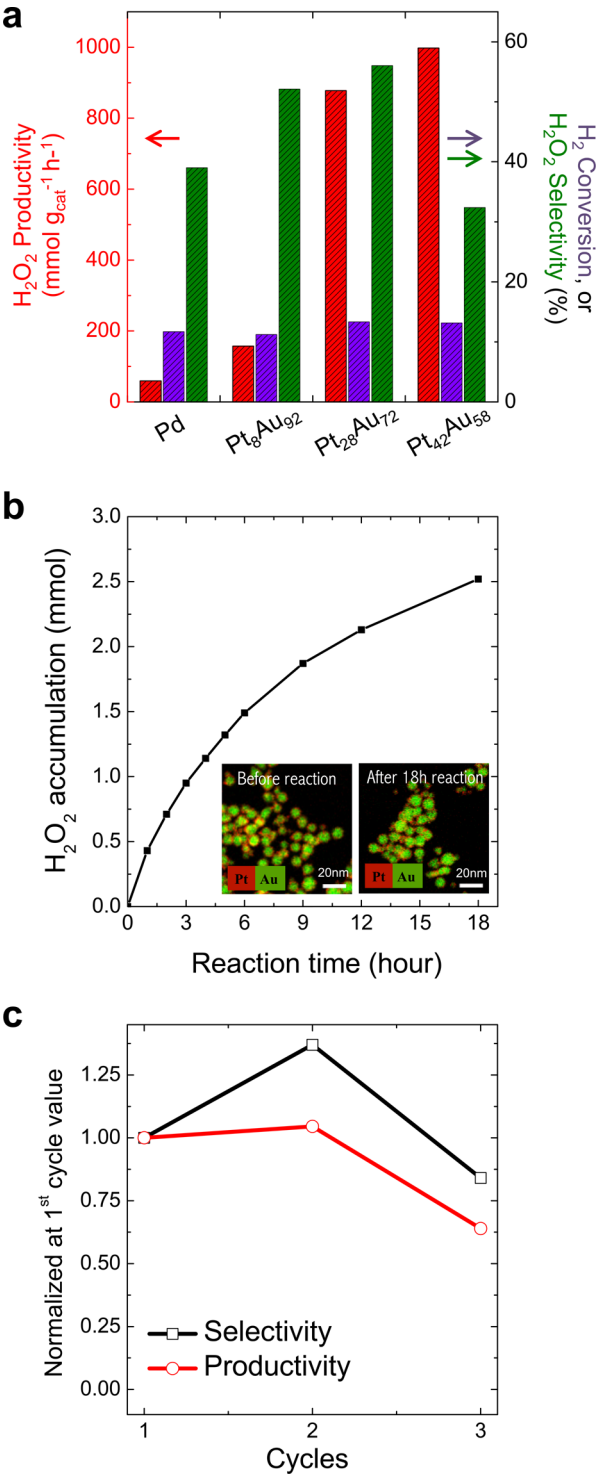

Figure 4. Isoconversion, long-term stability, and reuse tests of PtAu NPs. (a) Isoconversion comparison of the catalytic performance of PtAu NPs and the reference Pd. The H_2 conversion value of each sample was controlled to reach ~12%: 11.72% (Pd), 11.22% (Pt_8Au_{92}), 13.34% ($Pt_{28}Au_{72}$), and 13.17% ($Pt_{42}Au_{58}$). (b) Accumulated concentration (mmol) of H_2O_2 produced with $Pt_{28}Au_{72}$ NPs over time (up to 18 h). The insets are the TEM-EDS maps of the collective $Pt_{28}Au_{72}$ NPs before and after the 18 h reaction. (c) Catalyst reuse tests of up to 3 times with $Pt_{28}Au_{72}$ NPs. Each productivity and selectivity were normalized at the first cycle value.

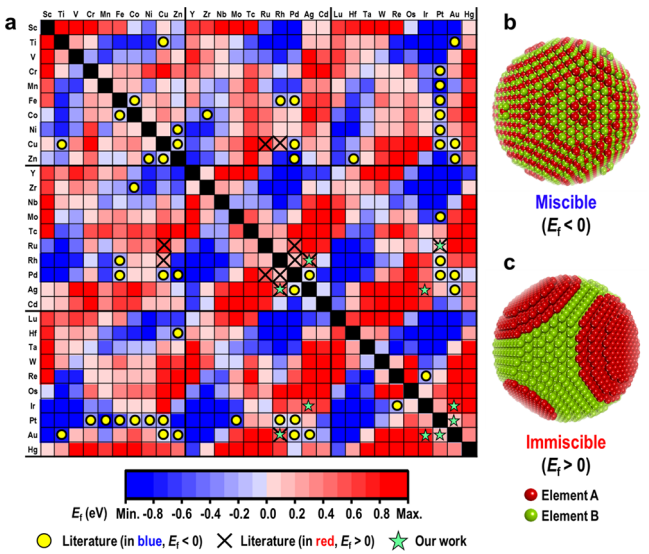

Figure 5. Positioning our catalysts in bimetallic catalyst map. (a) Bimetallic catalyst map based on alloy formation energies (E_f). Circles in yellow represent previous works in literature that report bimetallic catalysts, while stars in green represent new points of the present work. References are provided as follows: (Co,Fe),[42] (Ni,Zn),[43] (Zn,Hf),[44] (Pd,Cu),[45,46] (Co,Pt),[47,48] (Pt,Ni),[48] (Pt,Re),[48] (Au,Cu),[48,49] (Pd,Zn),[48] (Pt,Mo),[48] (Ir,Re),[50] (Pd,Ag),[51] (Au,Ti),[52] (Pd,Au),[53] (Co,Zr),[54] (Cu,Zn),[55] (Pd,Fe),[56] (Cr,Pt),[57] (Mn,Pt),[58] (Fe,Pt),[57,58] (Au,Ag),[59,60] (Pt,Cu),[61] (Cu,Ti),[62] (Rh,Fe),[63] (Pd,Pt),[12,64] (Au,Zn),[65] (Rh,Pt),[66] (Ru,Cu),[67] (Pd,Ru),[68] (Cu,Rh),[69] (Pd,Rh),[70] (Rh,Ag),[71−73] and (Rh,Au).[73,74] (b, c) Schematics of nanoparticles of (b) each miscible (E_f < 0) or (c) immiscible (E_f > 0) elemental combination.

lations (our own) and dozens of literature results. A total of 435 binary alloys (1:1 composition only) consisting of transition metals in periods IV, V, and VI are considered. For each elemental combination, 10 thermodynamic phases were investigated: $L1_0$, B2, B1, B4, B3, B33, B11, B19, B27, and $L1_1$ (Figure S16 in the Supporting Information). The energies of all 10 phases were compared (Figures S17 and S18 in the Supporting Information), and only the most stable phase was presented. Clearly, two regions are distinguished by color in the map: one for negative E_f (in blue) and the other for positive E_f (in red). The former indicates that the intermixing of two elements is thermodynamically favorable whereas the latter means the opposite. The resulting nanostructures should also differ significantly. The former will lead to a miscible alloy (Figure 5b) where two elements are homogeneously mixed at the atomic level, while separated domains of each element would preferably dominate for the latter (Figure 5c). The novel catalysts (RhAg, RhAu, PtAu, and IrAg) presented in this work all belong to the latter.

Actual examples of bimetallic catalysts that have been reported so far are collected from the literature[42−74] and highlighted on the map (Figure 5a). One can observe that previous efforts to search for bimetallic catalysts have been highly biased, as they are mostly found in the region of negative E_f (yellow circles in blue region). On the other hand, the other material space of positive E_f (red region of Figure 5a) has been relatively much disregarded for catalyst developments, although it occupies more than half (58%, Table S7) of the map. This is likely due to the inherent difficulty of alloy synthesis and stabilization for immiscible elemental combinations. In this work, we explore the underutilized space of bulk-immiscible combinations (red region of the map) to develop

DOI: 10.1021/acscatal.9b00451
ACS Catal. 2019, 9, 8702−8711

high-performance catalysts for H_2O_2 productions and successfully add new points (stars in green) on the map.

Importantly note a few recent efforts and success of solid-solution alloy synthesis of bulk-immiscible elements. Examples include Ru−Cu,[67] Pd−Ru,[68] and Cu−Rh[69] for CO or NO_x conversion and Pd−Rh,[70] Rh−Ag,[71−73] and Rh−Au[73,74] for hydrogen storage or hydrogenation catalysts (× marks on the map). However, these works are conceptually different from ours; here we clarify the difference. In their reports, NPs of bulk-immiscible elements are formed in a solid-solution alloy structure, enabled by nanosize or promoter effects. In contrast, our NPs are characterized by segregated domains of each element. We demonstrate that synergistic catalytic effects can occur at the interfaces between elemental domains even for segregated alloy NPs. Because such segregations would naturally be observed for most bulk-immiscible elements, our work would substantially increase the scope of future explorations of improved catalyst materials.

4. CONCLUSIONS

We use the material space of bulk-immiscible elements to discover H_2O_2-producing catalysts. As a result of a combined approach of DFT calculations and catalytic experiments, novel bimetallic catalysts based on immiscible elemental combinations of Rh−Ag, Rh−Au, Pt−Au, and Ir−Ag are demonstrated to efficiently produce H_2O_2, despite the negligible activities of Rh, Pt, Ir, Ag, and Au alone. The two catalysts $Rh_{13}Ag_{87}$ NPs and $Pt_{28}Au_{72}$ NPs are the primary outcomes. The former ($Rh_{13}Ag_{87}$ NPs) exhibits the largest CNP (13.3 mmol $\$_{cat}^{-1}$ h^{-1}), which is ∼7.3 times higher than that of the Pd sample and thus may serve as an economical option. The latter ($Pt_{28}Au_{72}$ NPs) shows a superior productivity of 300 mmol g_{cat}^{-1} h^{-1} and a 15-fold increase over that of Pd under isoconversion conditions. These catalysts additionally offer the benefit of a long lifetime (>18 h). This work avoids using Pd element for H_2O_2 synthesis and instead utilizes the combination and synergy of Ag, Au, Rh, Ir, and Pt, each of which is known to individually perform poorly for H_2O_2 production. We highlight that our work opens a route for new catalyst developments in the less-explored space (bulk-immiscible elements) of the bimetallic catalyst map; it will hopefully stimulate more active utilizations of the space.

■ ASSOCIATED CONTENT

Supporting Information

The Supporting Information is available free of charge on the ACS Publications website at DOI: 10.1021/acscatal.9b00451.

Details and additional results on the DFT calculations and the experiments (PDF)

■ AUTHOR INFORMATION

Corresponding Authors

*E-mail: kylee@korea.ac.kr.
*E-mail: patra@kist.re.kr.
*E-mail: sangsoo@kist.re.kr.

ORCID

Donghun Kim: 0000-0003-0326-5381
So-Hye Cho: 0000-0001-9707-8629
Kwan-Young Lee: 0000-0002-5637-1009
Sang Soo Han: 0000-0002-7925-8105

Author Contributions

#D.K., H.N., Y.-H.C., and B.C.Y. contributed equally.

Notes

The authors declare no competing financial interest.

■ ACKNOWLEDGMENTS

This work was supported by Creative Materials Discovery Program through the National Research Foundation of Korea (NRF-2016M3D1A1021140) and the Korea Institute of Science and Technology (Grant no. 2E29280). The authors are grateful to Hong Woo Lee for helping to illustrate the figures.

■ REFERENCES

(1) *Ulmann's Encyclopedia of Industrial Chemistry*; Wiley: 1999−2013.
(2) Edwards, J. K.; Hutchings, G. J. Palladium and Gold-Palladium Catalysts for the Direct Synthesis of Hydrogen Peroxide. *Angew. Chem., Int. Ed.* **2008**, *47*, 9192−9198.
(3) Pfleiderer, G.; Reidl, H.-J. Production of Hydrogen Peroxide. U.S. Patent 2,158,525, 1939.
(4) Henkel, H.; Weber, W. Manufacture of Hydrogen Peroxide. U.S. Patent 1,108,752, 1914.
(5) Dissanayake, D. P.; Lunsford, J. H. Evidence for the Role of Colloidal Palladium in the Catalytic Formation of H_2O_2 from H_2 and O_2. *J. Catal.* **2002**, *206*, 173−176.
(6) Lunsford, J. H. The Direct Formation of H_2O_2 from H_2 and O_2 over Palladium Catalysts. *J. Catal.* **2003**, *216*, 455−460.
(7) Solsona, B. E.; Edwards, J. K.; Landon, P.; Carley, A. F.; Herzing, A.; Kiely, C. J.; Hutchings, G. J. Direct Synthesis of Hydrogen Peroxide from H_2 and O_2 Using Al_2O_3 Supported Au-Pd Catalysts. *Chem. Mater.* **2006**, *18*, 2689−2695.
(8) Edwards, J. K.; Solsona, B.; Ntainjua N, E.; Carley, A. F.; Herzing, A. A.; Kiely, C. J.; Hutchings, G. J. Switching Off Hydrogen Peroxide Hydrogenation in the Direct Synthesis Process. *Science* **2009**, *323*, 1037−1041.
(9) Edwards, J. K.; Pritchard, J.; Piccinini, M.; Shaw, G.; He, Q.; Carley, A. F.; Kiely, C. J.; Hutchings, G. J. The Effect of Heat Treatment on the Performance and Structure of Carbon-Supported Au-Pd Catalysts for the Direct Synthesis of Hydrogen Peroxide. *J. Catal.* **2012**, *292*, 227−238.
(10) Edwards, J. K.; Parker, S. F.; Pritchard, J.; Piccinini, M.; Freakley, S. J.; He, Q.; Carley, A. F.; Kiely, C. J.; Hutchings, G. J. Effect of Acid Pre-treatment on AuPd/SiO_2 Catalysts for the Direct Synthesis of Hydrogen Peroxide. *Catal. Sci. Technol.* **2013**, *3*, 812−818.
(11) Edwards, J. K.; Freakley, S. J.; Carley, A. F.; Kiely, C. J.; Hutchings, G. J. Strategies for Designing Supported Gold-Palladium Bimetallic Catalysts for the Direct Synthesis of Hydrogen Peroxide. *Acc. Chem. Res.* **2014**, *47*, 845−854.
(12) Sterchele, S.; Biasi, P.; Centomo, P.; Canton, P.; Campestrini, S.; Salmi, T.; Zecca, M. Pd-Au and Pd-Pt Catalysts for the Direct Synthesis of Hydrogen Peroxide in Absence of Selectivity Enhancers. *Appl. Catal., A* **2013**, *468*, 160−174.
(13) Freakley, S. J.; He, Q.; Harrhy, J. H.; Lu, L.; Crole, D. A.; Morgan, D. J.; Ntainjua, D. N.; Edwards, J. K.; Carley, A. F.; Borisevich, A. Y.; Kiely, C. J.; Hutchings, G. J. Palladium-Tin Catalysts for the Direct Synthesis of H_2O_2 with High Selectivity. *Science* **2016**, *351*, 965−968.
(14) Siahrostami, S.; Verdaguer-Casadevall, A.; Karamad, M.; Deiana, D.; Malacrida, P.; Wickman, B.; Escudero-Escribano, M.; Paoli, E. A.; Frydendal, R.; Hansen, T. W.; Chorkendorff, I.; Stephens, I. E. L.; Rossmeisl, J. Enabling Direct H_2O_2 Production Through Rational Electrocatalyst Design. *Nat. Mater.* **2013**, *12*, 1137−1143.
(15) Maity, S.; Eswaramoorthy, M. Ni-Pd Bimetallic Catalysts for the Direct Synthesis of H_2O_2 - Unusual Enhancement of Pd Activity in the Presence of Ni. *J. Mater. Chem. A* **2016**, *4*, 3233−3237.

DOI: 10.1021/acscatal.9b00451
ACS Catal. 2019, 9, 8702−8711

(16) Kresse, G.; Furthmuller, J. Efficiency of *Ab-initio* Total Energy Calculations for Metals and Semiconductors Using a Plane-Wave Basis Set. *Comput. Mater. Sci.* **1996**, *6*, 15−50.
(17) Hammer, B.; Hansen, L. B.; Nørskov, J. K. Improved Adsorption Energetics within Density-Functional Theory Using Revised Perdew-Burke-Ernzerhof Functionals. *Phys. Rev. B: Condens. Matter Mater. Phys.* **1999**, *59*, 7413−7421.
(18) Kresse, G.; Joubert, D. From Ultrasoft Pseudopotentials to the Projector Augmented-Wave Method. *Phys. Rev. B: Condens. Matter Mater. Phys.* **1999**, *59*, 1758−1775.
(19) Sheppard, D.; Terrell, R.; Henkelman, G. Optimization Methods for Finding Minimum Energy Paths. *J. Chem. Phys.* **2008**, *128*, No. 134106.
(20) Mulfinger, l.; Solomon, S. D.; Bahadory, M.; Jeyarajasingam, A. V.; Rutkowsky, S. A.; Boritz, C. Synthesis and Study of Silver Nanoparticles. *J. Chem. Educ.* **2007**, *84*, 322−325.
(21) Jin, M.; Liu, H.; Zhang, H.; Xie, Z.; Liu, J.; Xia, Y. Synthesis of Pd Nanocrystals Enclosed by {100} Facets and with Sizes < 10 nm for Application in CO Oxidation. *Nano Res.* **2011**, *4*, 83−91.
(22) Samanta, C. Direct Synthesis of Hydrogen Peroxide from Hydrogen and Oxygen: An Overview of Recent Developments in the Process. *Appl. Catal., A* **2008**, *350*, 133−149.
(23) Han, Y.-F.; Lunsford, J. H. A Comparison of Ethanol and Water as the Liquid Phase in the Direct Formation of H_2O_2 from H_2 and O_2 over a Palladium Catalyst. *Catal. Lett.* **2005**, *99*, 13−19.
(24) Li, J.; Staykov, A.; Ishihara, T.; Yoshizawa, K. Theoretical Study of the Decomposition and Hydrogenation of H_2O_2 on Pd and Au@Pd Surfaces: Understanding toward High Selectivity of H_2O_2 Synthesis. *J. Phys. Chem. C* **2011**, *115*, 7392−7398.
(25) Seo, D.-H.; Shin, H.; Kang, K.; Kim, H.; Han, S. S. First-Principles Design of Hydrogen Dissociation Catalysts Based on Isoelectronic Metal Solid Solutions. *J. Phys. Chem. Lett.* **2014**, *5*, 1819−1824.
(26) Li, B.; Ding, Y.; Kim, D. Y.; Ahuja, R.; Zou, G.; Mao, H.-K. Rhodium Dihydride (RhH_2) with High Volumetric Hydrogen Density. *Proc. Natl. Acad. Sci. U. S. A.* **2011**, *108*, 18618−18621.
(27) Fajin, J. S. C.; Cordeiro, M. N. D. S.; Gomes, J. R. B. On the Theoretical Understanding of the Unexpected O_2 Activation by Nanoporous Gold. *Chem. Commun.* **2011**, *47*, 8403−8405.
(28) Xu, Y.; Mavrikakis, M. Adsorption and Dissociation of O_2 on Gold Surfaces: Effect of Steps and Strain. *J. Phys. Chem. B* **2003**, *107*, 9298−9307.
(29) Goikoetxea, I.; Beltran, J.; Meyer, J.; Inaki Juaristi, J.; Alducin, M.; Reuter, K. Non-Adiabatic Effects During the Dissociative Adsorption of O_2 at Ag(111)? A First-Principles Divide and Conquer Study. *New J. Phys.* **2012**, *14*, No. 013050.
(30) Loncaric, I.; Alducin, M.; Juaristi, J. I. Dissociative Dynamics of O_2 on Ag(110). *Phys. Chem. Chem. Phys.* **2015**, *17*, 9436−9445.
(31) Choudhary, V. R.; Samanta, C.; Choudhary, T. V. Direct Oxidation of H_2 to H_2O_2 over Pd-Based Catalysts: Influence of Oxidation State, Support and Metal Additives. *Appl. Catal., A* **2006**, *308*, 128−133.
(32) Peng, Z.; You, H.; Yang, H. Composition-Dependent Formation of Platinum Silver Nanowires. *ACS Nano* **2010**, *4*, 1501−1510.
(33) Pan, Y.-T.; Yan, Y.; Shao, Y.-T.; Zuo, J.-M.; Yang, H. Ag-Pt Compositional Intermetallics Made from Alloy Nanoparticles. *Nano Lett.* **2016**, *16*, 6599−6603.
(34) Verhallen, P. T. H. M.; Oomen, L. J. P.; Elsen, A. J. J. M. v. d.; Kruger, J.; Fortuin, J. M. H. The Diffusion Coefficients of Helium, Hydrogen, Oxygen and Nitrogen in Water Determined from the Permeability of a Stagnant Liquid Layer in the Quasi-s. *Chem. Eng. Sci.* **1984**, *39*, 1535−1541.
(35) Fiévet, F.; Brayner, R. The Polyol Process. In *Nanomaterials: A Danger or a Promise?*; Springer: London, 2013; pp 1−25.
(36) Bratsch, S. G. Standard Electrode Potentials and Temperature Coefficients in Water at 298.15 K. *J. Phys. Chem. Ref. Data* **1989**, *18*, 1−21.
(37) Kim, S.; Lee, D.-W.; Lee, K.-Y. Direct Synthesis of Hydrogen Peroxide from Hydrogen and Oxygen over Single-Crystal Cubic Palladium on Silica Catalysts. *J. Mol. Catal. A: Chem.* **2014**, *383*, 64−69.
(38) Kim, S.; Lee, D.-W.; Lee, K.-Y. Shape-Dependent Catalytic Activity of Palladium Nanoparticles for the Direct Synthesis of Hydrogen Peroxide from Hydrogen and Oxygen. *J. Mol. Catal. A: Chem.* **2014**, *391*, 48−54.
(39) Edwards, J. K.; Solsona, B. E.; Landon, P.; Carley, A. F.; Herzing, A.; Kiely, C. J.; Hutchings, G. J. Direct Synthesis of Hydrogen Peroxide from H_2 and O_2 Using TiO_2-Supported Au-Pd Catalysts. *J. Catal.* **2005**, *236*, 69−79.
(40) Plauck, A.; Stangland, E. E.; Dumesic, J. A.; Mavrikakis, M. Active Sites and Mechanisms for H_2O_2 Decomposition over Pd Catalysts. *Proc. Natl. Acad. Sci. U. S. A.* **2016**, *113*, E1973−E1982.
(41) Metal prices slightly change on a daily basis, and therefore the CNP value will also change accordingly. The prices can be reached from the InvestmentMine webpage (http://www.infomine.com/investment/metal-prices/). Prices of a few select metals (as of Nov. 6, 2017) are as follows: 45.81 $/g (Rh), 40.80 $/g (Au), 32.23 $/g (Pd), 31.19 $/g (Ir), 29.64 $/g (Pt), and 0.54 $/g (Ag).
(42) Gnanamani, M. K.; Jacobs, G.; Hamdeh, H. H.; Shafer, W. D.; Liu, F.; Hopps, S. D.; Thomas, G. A.; Davis, B. H. Hydrogenation of Carbon Dioxide over Co-Fe Bimetallic Catalysts. *ACS Catal.* **2016**, *6*, 913−927.
(43) Al-ShaikhAli, A. H.; Jedidi, A.; Anjum, D. H.; Cavallo, L.; Takanabe, K. Kinetics on NiZn Bimetallic Catalysts for Hydrogen Evolution via Selective Dehydrogenation of Methylcyclohexane to Toluene. *ACS Catal.* **2017**, *7*, 1592−1600.
(44) De Baerdemaeker, T.; Feyen, M.; Muller, U.; Yilmaz, B.; Xiao, F.-S.; Zhang, W.; Yokoi, T.; Bao, X.; Gies, H.; De Vos, D. E. Bimetallic Zn and Hf on Silica Catalysts for the Conversion of Ethanol to 1,3-Butadiene. *ACS Catal.* **2015**, *5*, 3393−3397.
(45) Jiang, X.; Koizumi, N.; Guo, X.; Song, C. Bimetallic Pd-Cu Catalysts for Selective CO_2 Hydrogenation to Methanol. *Appl. Catal., B* **2015**, *170*−*171*, 173−185.
(46) Zhang, S.; Kang, P.; Bakir, M.; Lapides, A. M.; Dares, C. J.; Meyer, T. J. Polymer-Supported CuPd Nanoalloy as a Synergistic Catalyst for Electrocatalytic Reduction of Carbon Dioxide to Methane. *Proc. Natl. Acad. Sci. U. S. A.* **2015**, *112*, 15809−15814.
(47) Guczi, L.; Boskovic, G.; Kiss, E. Bimetallic Cobalt Based Catalysts. *Catal. Rev.: Sci. Eng.* **2010**, *52*, 133−203.
(48) Wei, Z.; Sun, J.; Li, Y.; Datye, A. K.; Wang, Y. Bimetallic Catalysts for Hydrogen Generation. *Chem. Soc. Rev.* **2012**, *41*, 7994−8008.
(49) Kim, D.; Resasco, J.; Yu, Y.; Asiri, A. M.; Yang, P. Synergistic Geometric and Electronic Effects for Electrochemical Reduction of Carbon Dioxide Using Gold-Copper Bimetallic Nanoparticles. *Nat. Commun.* **2014**, *5*, No. 4948.
(50) Deng, C.; Duan, X.; Zhou, J.; Zhou, X.; Yuan, W.; Scott, S. L. Ir-Re Alloy as a Highly Active Catalyst for the Hydrogenolysis of Glycerol to 1,3-Propanediol. *Catal. Sci. Technol.* **2015**, *5*, 1540−1547.
(51) Zhang, Y.; Diao, W.; Monnier, J. R.; Williams, C. T. Pd-Ag/SiO_2 Bimetallic Catalysts Prepared by Galvanic Displacement for Selective Hydrogenation of Acetylene in Excess Ethylene. *Catal. Sci. Technol.* **2015**, *5*, 4123−4132.
(52) Bang, K.; Shin, K.; Ryu, M. S.; Kwon, S.; Lee, H. M. Titanium-Promoted Au-Ti Bimetallic Nanoparticle Catalysts for CO Oxidation: A Theoretical Approach. *Catal. Today* **2016**, *265*, 14−18.
(53) Gao, F.; Goodman, D. W. Pd-Au Bimetallic Catalysts: Understanding Alloy Effects from Planar Models and (Supported) Nanoparticles. *Chem. Soc. Rev.* **2012**, *41*, 8009−8020.
(54) Zhang, G.; Hao, L.; Jia, Y.; Du, Y.; Zhang, Y. CO_2 Reforming of CH_4 over Efficient Bimetallic Co-Zr/AC Catalyst for H_2 Production. *Int. J. Hydrogen Energy* **2015**, *40*, 12868−12879.
(55) Wang, Z.; Wang, G.; Louis, C.; Delannoy, L. Novel Non-noble Bimetallic Cu-Zn/TiO_2 Catalysts for Selective Hydrogenation of Butadiene. *J. Catal.* **2017**, *347*, 185−196.

DOI: 10.1021/acscatal.9b00451
ACS Catal. 2019, 9, 8702−8711

(56) Sun, J.; Karim, A. M.; Zhang, H.; Kovarik, L.; Li, X. S.; Hensley, A. J.; McEwen, J.-S.; Wang, Y. Carbon-Supported Bimetallic Pd-Fe Catalysts for Vapor-Phase Hydrodeoxygenation of Guaiacol. *J. Catal.* **2013**, *306*, 47−57.
(57) Niaei, A.; Salari, D.; Aghazadeh, F.; Caylak, N.; Sepehrianazar, A. Catalytic Oxidation of 2-Propanol over (Cr,Mn,Fe)-Pt/Al_2O_3 Bimetallic Catalysts and Modeling of Experimental Results by Artificial Neural Networks. *J. Environ. Sci. Health, Part A: Toxic/Hazard. Subst. Environ. Eng.* **2010**, *45*, 454−463.
(58) Xiang, D.; Yin, L. Well-Dispersed and Size-Tuned Bimetallic $PtFe_x$ Nanoparticle Catalysts Supported on Ordered Mesoporous Carbon for Enhanced Electrocatalytic Activity in Direct Methanol Fuel Cells. *J. Mater. Chem.* **2012**, *22*, 9584−9593.
(59) Rodriguez-Gonzalez, B.; Burrows, A.; Watanabe, M.; Kiely, C. J.; Liz Marzan, L. M. Multishell Bimetallic AuAg Nanoparticles: Synthesis, Structure and Optical Properties. *J. Mater. Chem.* **2005**, *15*, 1755−1759.
(60) Wang, A.-Q.; Chang, C.-M.; Mou, C.-Y. Evolution of Catalytic Activity of Au-Ag Bimetallic Nanoparticles on Mesoporous Support for CO Oxidation. *J. Phys. Chem. B* **2005**, *109*, 18860−18867.
(61) Han, Z.; Li, S.; Jiang, F.; Wang, T.; Ma, X.; Gong, J. Propane Dehydrogenation over Pt-Cu Bimetallic Catalysts: The Nature of Coke Deposition and the Role of Copper. *Nanoscale* **2014**, *6*, 10000−10008.
(62) Lu, Q.; Hutchings, G. S.; Yu, W.; Zhou, Y.; Forest, R. V.; Tao, R.; Rosen, J.; Yonemoto, B. T.; Cao, Z.; Zheng, H.; Xiao, J. Q.; Jiao, F.; Chen, J. G. Highly Porous Non-precious Bimetallic Electrocatalysts for Efficient Hydrogen Evolution. *Nat. Commun.* **2015**, *6*, No. 6567.
(63) Chen, H.; Lu, Q.; Yi, C.; Yang, B.; Qi, S. Bimetallic Rh-Fe Catalysts for N_2O Decomposition: Effects of Surface Structures on Catalytic Activity. *Phys. Chem. Chem. Phys.* **2018**, *20*, 5103−5111.
(64) Ye, H.; Crooks, R. M. Effect of Elemental Composition of PtPd Bimetallic Nanoparticles Containing an Average of 180 Atoms on the Kinetics of the Electrochemical Oxygen Reduction Reaction. *J. Am. Chem. Soc.* **2007**, *129*, 3627−3633.
(65) Campos, L. C.; Tonezzer, M.; Ferlauto, A. S.; Grillo, V.; Magalhães-Paniago, R.; Oliveira, S.; Ladeira, L. O.; Lacerda, R. G. Vapor-Solid-Solid Growth Mechanism Driven by Epitaxial Match between Solid AuZn Alloy Catalyst Particles and ZnO Nanowires at Low Temperatures. *Adv. Mater.* **2008**, *20*, 1499−1504.
(66) Alayoglu, S.; Eichhorn, B. Rh-Pt Bimetallic Catalysts: Synthesis, Characterization, and Catalysis of Core-Shell, Alloy, and Monometallic Nanoparticles. *J. Am. Chem. Soc.* **2008**, *130*, 17479−17486.
(67) Huang, B.; Kobayashi, H.; Yamamoto, T.; Matsumura, S.; Nishida, Y.; Sato, K.; Nagaoka, K.; Kawaguchi, S.; Kubota, Y.; Kitagawa, H. Solid-Solution Alloying of Immiscible Ru and Cu with Enhanced CO Oxidation Activity. *J. Am. Chem. Soc.* **2017**, *139*, 4643−4646.
(68) Kusada, K.; Kobayashi, H.; Ikeda, R.; Kubota, Y.; Takata, M.; Toh, S.; Yamamoto, T.; Matsumura, S.; Sumi, N.; Sato, K.; Nagaoka, K.; Kitagawa, H. Solid Solution Alloy Nanoparticles of Immiscible Pd and Ru Elements Neighboring on Rh: Changeover of the Thermodynamic Behavior for Hydrogen Storage and Enhanced CO-Oxidizing Ability. *J. Am. Chem. Soc.* **2014**, *136*, 1864−1871.
(69) Komatsu, T.; Kobayashi, H.; Kusada, K.; Kubota, Y.; Takata, M.; Yamamoto, T.; Matsumura, S.; Sato, K.; Nagaoka, K.; Kitagawa, H. First-Principles Calculation, Synthesis, and Catalytic Properties of Rh-Cu Alloy Nanoparticles. *Chem. - Eur. J.* **2017**, *23*, 57−60.
(70) Kobayashi, H.; Morita, H.; Yamauchi, M.; Ikeda, R.; Kitagawa, H.; Kubota, Y.; Kato, K.; Takata, M.; Toh, S.; Matsumura, S. Nanosize-Induced Drastic Drop in Equilibrium Hydrogen Pressure for Hydride Formation and Structural Stabilization in Pd-Rh Solid-Solution Alloys. *J. Am. Chem. Soc.* **2012**, *134*, 12390−12393.
(71) Kusada, K.; Yamauchi, M.; Kobayashi, H.; Kitagawa, H.; Kubota, Y. Hydrogen-Storage Properties of Solid-Solution Alloys of Immiscible Neighboring Elements with Pd. *J. Am. Chem. Soc.* **2010**, *132*, 15896−15898.
(72) Kunal, P.; Roberts, E. J.; Riche, C. T.; Jarvis, K.; Malmstadt, N.; Brutchey, R. L.; Humphrey, S. M. Continuous Flow Synthesis of Rh and RhAg Alloy Nanoparticle Catalysts Enables Scalable Production and Improved Morphological Control. *Chem. Mater.* **2017**, *29*, 4341−4350.
(73) Garcia, S.; Zhang, L.; Piburn, G. W.; Henkelman, G.; Humphrey, S. M. Microwave Synthesis of Classically Immiscible Rhodium-Silver and Rhodium-Gold Alloy Nanoparticles: Highly Active Hydrogenation Catalysts. *ACS Nano* **2014**, *8*, 11512−11521.
(74) Li, H.; Luo, L.; Kunal, P.; Bonifacio, C. S.; Duan, Z.; Yang, J. C.; Humphrey, S. M.; Crooks, R. M.; Henkelman, G. Oxygen Reduction Reaction on Classically Immiscible Bimetallics: A Case Study of RhAu. *J. Phys. Chem. C* **2018**, *122*, 2712−2716.

DOI: 10.1021/acscatal.9b00451
ACS Catal. 2019, 9, 8702−8711